Journal of Materials Chemistry C

ROYAL SOCIETY OF CHEMISTRY

PAPER

View Article Online
View Journal | View Issue

Cite this: J. Mater. Chem. C, 2025, 13, 19626

An ultra-low dark current, high-performance photodetector based on CVD-grown Bi_2TeO_5

Yunxiao Min,[ab] Jie Liu,[c] Zihan Wang[ab] and Liang Li *[a]

Received 9th April 2025,
Accepted 11th August 2025

DOI: 10.1039/d5tc01483b

rsc.li/materials-c

Low-dimensional materials, particularly quasi-2D semiconductors like bismuth oxychalcogenides (BiOX), offer unique advantages for advanced photodetection due to van der Waals integration and quantum-confined properties. In this research, Bi_2TeO_5 nanosheets were successfully grown using a chemical vapor deposition method. The resulting Bi_2TeO_5 photodetector exhibited remarkable performance characteristics. Specifically, it demonstrated an open circuit voltage of −1.14 V, a depolarization field of 5.7×10^7 V m^{-1}, a remarkably low dark current of 10^{-15} A, an impressive on/off ratio of 10^3, a responsivity of 466.80 mA W^{-1}, a detectivity of 4.23×10^{12} Jones, and an EQE of 218.44% at 8 V bias. The work highlights the significant potential of Bi_2TeO_5 and provides new design strategies for developing next-generation 2D photodetectors.

Introduction

Low-dimensional materials possess unique properties, making them strong alternatives to traditional photodetection materials. The interlayer connections in two-dimensional (2D) materials are facilitated by van der Waals forces, which effectively address the lattice mismatch issue between substrates and materials, thereby simplifying integration and processing procedures.[1–5] Furthermore, when materials are scaled down to the nanoscale, their energy band structure transitions from quasi-continuous to discrete quantum energy levels, leading to changes in absorbed photon energy and bandgap width.[6–9] These defining characteristics distinguish low-dimensional materials from bulk materials, opening up exciting possibilities for optoelectronic detection technologies. In recent years, a new class of quasi-2D semiconductor materials—bismuth oxychalcogenides (BiOX, X = S, Se, Te)—has been demonstrated to exhibit outstanding optoelectronic properties.[10–16]

Within the bismuth oxychalcogenide family, Bi_2TeO_5 crystals were identified as classic nonlinear optical (NLO) materials as early as the 1980s and subsequently studied.[17,18] Research by López *et al.* revealed that Bi_2TeO_5 crystallizes in an orthorhombic structure with the space group *Aem*2. This structure features BiO_3, Bi_2O_5, and Bi_3O_3 polyhedra sharing vertices with TeO_3 trigonal pyramids, arranged in a three-layer configuration. The stereochemically active lone-pair electrons of Bi^{3+} and Te^{4+} cations are oriented away from the strong covalent bonds. Crucially, the uncompensated lone-pair electrons of Bi^{3+} throughout the structure are responsible for the NLO properties of Bi_2TeO_5.[19] Furthermore, Bi_2TeO_5 is renowned for its excellent air stability and thermal resistance, maintaining its phase stability at temperatures exceeding 900 °C. Its (100) plane is a cleavable surface, and the material exhibits a band gap of 3.21 eV. Bulk Bi_2TeO_5 possesses properties including photorefractivity, photochromism, photoelectric effects, and holographic memory capabilities.[20–25]

Following the exploration of Bi_2SeO_5 as a 2D dielectric for device fabrication, structurally similar 2D Bi_2TeO_5 has also garnered research interest. Han *et al.* grew 2D Bi_2TeO_5 on mica substrates *via* chemical vapor deposition (CVD) for ferroelectric characterization. Density functional theory calculations indicated the presence of glide-mirror symmetry in the Bi_2TeO_5 monolayer. A cooperative mechanism involving a 0.11 Å displacement of Bi^{3+} cations along the *a*-axis and a 40° rotation of BiO_5 polyhedra around the *b*-axis induces an in-plane spontaneous polarization along the *a*-axis through atomic-scale reconstruction.[26] Kumar *et al.* synthesized 2D Bi_2TeO_5 flakes of varying thicknesses using a microwave-assisted method, demonstrating the feasibility of Bi_2TeO_5 nanosheets for photodetector applications.[27] Li *et al.* optimized CVD parameters using a disordered bismuth tellurite buffer layer, enabling the growth of Bi_2TeO_5 nanosheets at a relatively low temperature (500 °C).[28] Zhang *et al.* successfully synthesized high-κ Bi_2TeO_5 nanosheets *via* CVD, which exhibited outstanding electrical performance in photogating configurations.[29] Nevertheless, research on the growth and optoelectronic properties of 2D Bi_2TeO_5 materials remains at a nascent stage.

[a] Key Laboratory of Materials Physics, Anhui Key Laboratory of Nanomaterials and Nanotechnology, Institute of Solid State Physics, Hefei Institutes of Physical Science, Chinese Academy of Sciences, Hefei 230031, P.R. China
[b] University of Science and Technology of China, Hefei 230026, P. R. China
[c] State Key Laboratory of Materials Processing and Die & Mould Technology, School of Materials Science and Engineering, Huazhong University of Science and Technology, Wuhan 430074, P.R. China

In this work, high quality Bi_2TeO_5 nanosheets with a band gap width of 3.49 eV were successfully synthesized through meticulous control of growth parameters, including temperature, time, and gas flow rate, utilizing CVD to grow on a substrate. Notably, they exhibited a remarkably low dark current of 10^{-15} A. Their responsivity (R) was 466.80 mA W^{-1} and the EQE reached 218.44% under 265 nm at 8 V. This work provides new ideas and research directions for further exploration and development of new materials for 2D photodetectors.

Results and discussion

The structure of Bi_2TeO_5 is illustrated along the c-axis in Fig. 1a. To enhance the clarity of its architecture, the BiO_5 cages, constructed by Bi^{3+} and O^{2-} ions, are distinctly highlighted within a blue frame. Layer "A" comprises BiO_5 cages interspersed with Te^{4+} atoms, while layer "B" consists of Bi^{3+} and O^{2-} atoms. The Bi_2TeO_5 structure exhibits a repetitive "–A–B–A–" pattern. Bulk Bi_2TeO_5 possesses a non-centrosymmetric orthorhombic crystal lattice belonging to the *Aem*2 space group.[19,25] From the lattice

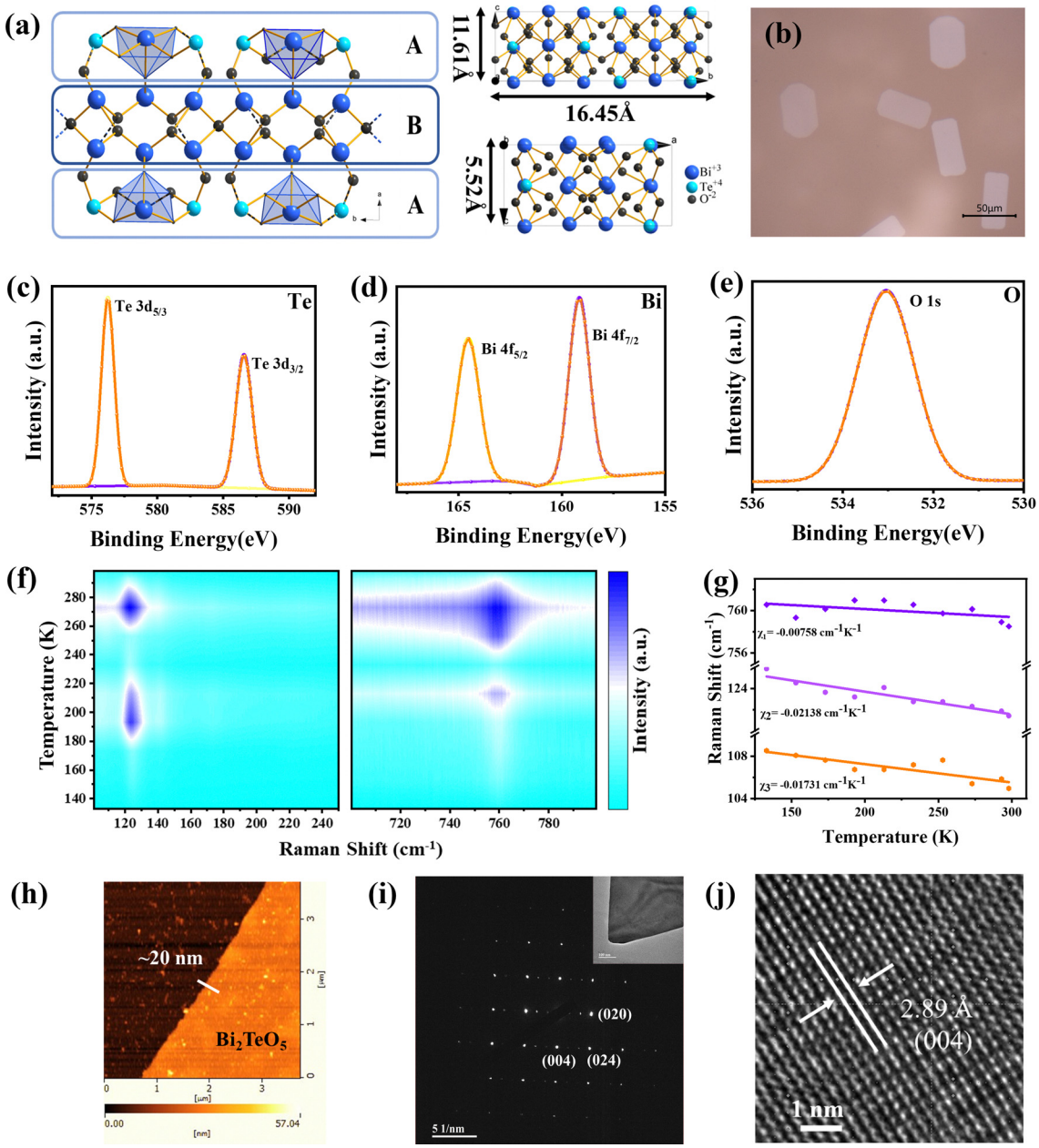

Fig. 1 (a) The structural diagram of the layered Bi_2TeO_5 structure along the different axes. (b) An optical image of the Bi_2TeO_5 nanosheet. The spectral characteristics of Te (c), Bi (d) and O (e) elements in the XPS spectra, respectively. (f) Variable-temperature Raman spectroscopy measurement diagram. (g) Fitting curve of the Raman peak position varying with temperature. (h) The AFM test results of Bi_2TeO_5. (i) SAED pattern of the Bi_2TeO_5 nanosheet, with an inset illustrating the measurement area. (j) HRTEM image of the same region of the Bi_2TeO_5 nanosheet.

structure of CollCode36446 in the ICSD, it can be known that the unit cell dimensions of Bi_2TeO_5 are a = 11.608 Å, b = 16.452 Å, and c = 5.518 Å and right angles ($\alpha = \beta = \gamma = 90^\circ$). An optical microscopy image of the Bi_2TeO_5 nanosheet grown on mica ($KMg_3(AlSi_3O_{10})F_2$) is presented in Fig. 1b, with dimensions of approximately 24 μm in width and 50 μm in length.

To characterize the composition and structure of the synthesized Bi_2TeO_5 nanosheets, a comprehensive array of analytical methods was employed. The valence state of Bi_2TeO_5 was precisely determined through X-ray photoelectron spectroscopy (XPS). The XPS spectra of the Te element (Fig. 1c) distinctly showcase two spin–orbit coupling splitting peaks positioned at 576.3 eV and 586.6 eV, corresponding to the core level peaks of the Te $3d_{5/2}$ and Te $3d_{3/2}$ states, respectively, indicating a Te^{4+} valence state. Similarly, in the XPS spectra of the Bi element (Fig. 1d), peaks located at 164.5 eV and 159.1 eV correspond to the Bi $4f_{5/2}$ and Bi $4f_{7/2}$ states, confirming a Bi^{3+} valence state. Additionally, the XPS spectra of the O element in Fig. 1e exhibit a peak at around 533.0 eV, representing the O 1s state and indicating an O^{2-} valence state.

A comprehensive Raman spectroscopic analysis was carried out using a 532 nm excitation laser (Fig. S1a, SI), revealing characteristic peaks of Bi_2TeO_5 at 110 cm^{-1} (assigned to the bending vibrations of the Te–O–Te bonds), 231 cm^{-1} (arising from the bending vibration of the Bi–O bonds), and 762 cm^{-1} (associated with the bending vibration of the Te–O bonds).[25] Fig. S1b, SI shows the Raman spectra of Bi_2TeO_5 nanosheets at a polarized light angle of 0°–180°. The initial angle of the polarizer is defined as 0°. With the increase of the polarization angle, the Raman peak intensity of the Bi_2TeO_5 nanosheet first increases and then decreases, reaching a relatively small value again at 90°. With the increase of the angle, the Raman peak intensity of the Bi_2TeO_5 nanosheet increases again and then decreases. Fig. S1c and S1d show characteristic peaks at 110 cm^{-1} and 762 cm^{-1}, respectively, with the polarization angle of 532 nm polarized light. The characteristic peaks with the polarization angle of the incident light indicate the asymmetry of the Bi_2TeO_5 nanosheets. To gain deeper insights into the vibrational dynamics of Bi_2TeO_5 nanosheets, temperature-dependent Raman spectroscopy was performed (Fig. 1f), covering a temperature range from 140 to 280 K. As the temperature increased, broadening of the full width at half maximum (FWHM) and a notable increase in peak intensity, particularly at 762 cm^{-1}, were observed. This phenomenon can be attributed to the suppression of lattice vibrations at lower temperatures, where photons excite more electrons to participate in scattering, resulting in a robust Raman scattering signal. However, as the temperature increases, thermal fluctuations promote electron excitation from their original energy levels to neighboring ones, broadening the Raman scattering and reducing the peak center intensity. Interestingly, the peak center intensity at room temperature exceeded that at lower temperatures, indicating an augmentation of the Raman cross-section for a specific vibrational mode. Notably, the peak at 231 cm^{-1} is not visible in Fig. 1f due to its relative weakness compared to the peak at 110 cm^{-1}. The relationship between the Raman peak positions and temperature was accurately described using the linear eqn (1).

$$\omega(T) = \omega_0 + \chi T \quad (1)$$

where T represents the testing temperature, ω_0 corresponds to the phonon frequency at 0 K, and χ signifies the first-order temperature coefficient. As presented in Fig. 1g, our results yield χ values of −0.00758, −0.02138, and −0.01731 cm^{-1} K^{-1} for the 110, 231, and 762 cm^{-1} peaks, respectively. These values strongly indicate the presence of a robust strain–phonon coupling within the Bi_2TeO_5 nanosheets.

As shown in Fig. 1h, the surface information of Bi_2TeO_5 nanosheets was characterized by atomic force microscopy (AFM). The measured thickness of Bi_2TeO_5 nanosheets was approximately 20 nm, with an arithmetic mean roughness (R_a) of 1.72 nm, indicating a relatively smooth surface and low microscopic inhomogeneity. The triangular projection of the nanosheet indicates the (111) crystal plane orientation. The selected area electron diffraction (SAED) pattern is shown in Fig. 1i, with the inset figure showing the measurement area, and with the zone axis ⟨001⟩, the sample distinctly exhibits a square symmetry, corresponding to the crystal faces (020), (004), and (024). The high-resolution transmission electron microscopy (HRTEM) image of the Bi_2TeO_5 nanosheet (Fig. 1j) reveals a crystal spacing of 2.89 Å, corresponding to crystallographic directions along (004). These HRTEM and SAED results further confirm the exceptional crystal quality of the Bi_2TeO_5 nanosheet. Fig. S1e–g, SI presents the corresponding energy dispersive spectrum (EDS) elemental mapping of the Bi_2TeO_5 nanosheet, revealing homogeneous distribution of Te, Bi and O elements that correlates well with the low-power TEM image in Fig. 1h. No additional elements were detected in the EDS analysis.

The synthesis of Bi_2TeO_5 nanosheets involved the utilization of Te powder and Bi_2O_3 powder in an Ar-rich environment, employing CVD techniques within the high-temperature zone of a tube furnace, as schematically shown in Fig. S2a, SI. As shown in Fig. 2, the ratio of Bi_2O_3 to the Te raw material plays an important role in the final growth of the material; when the ratio of Bi_2O_3 : Te was 5 : 1, the grown material was Bi_2O_3. With an increase in the proportion of Te in raw materials, when the ratio of Bi_2O_3 : Te was 1 : 1, the material grown started to become Bi_2TeO_5, but the size of Bi_2TeO_5 was small. Further increasing the Te proportion to a Bi_2O_3 : Te ratio of 1 : 5 enabled the growth of a larger size Bi_2TeO_5 material. The precursor ratio is decisive for Bi_2TeO_5 growth, with a significantly higher Te proportion being optimal. The crystallization process of Bi_2TeO_5 nanosheets can be seen from the change of growth time. First, regular massive nanosheets are formed after crystallization nucleation. With the increase of the growth time, the thickness of the Bi_2TeO_5 nanosheets increases along the (001) direction, while the area spreads around, and the growth rate in the (001) direction is greater than that of the (100) and (010) directions. No significant morphological differences were observed microscopically within 30 min. However, when the growth time reached 40 min or above, the nanosheets showed a tetrahedral shape, consistent with the TEM projection:

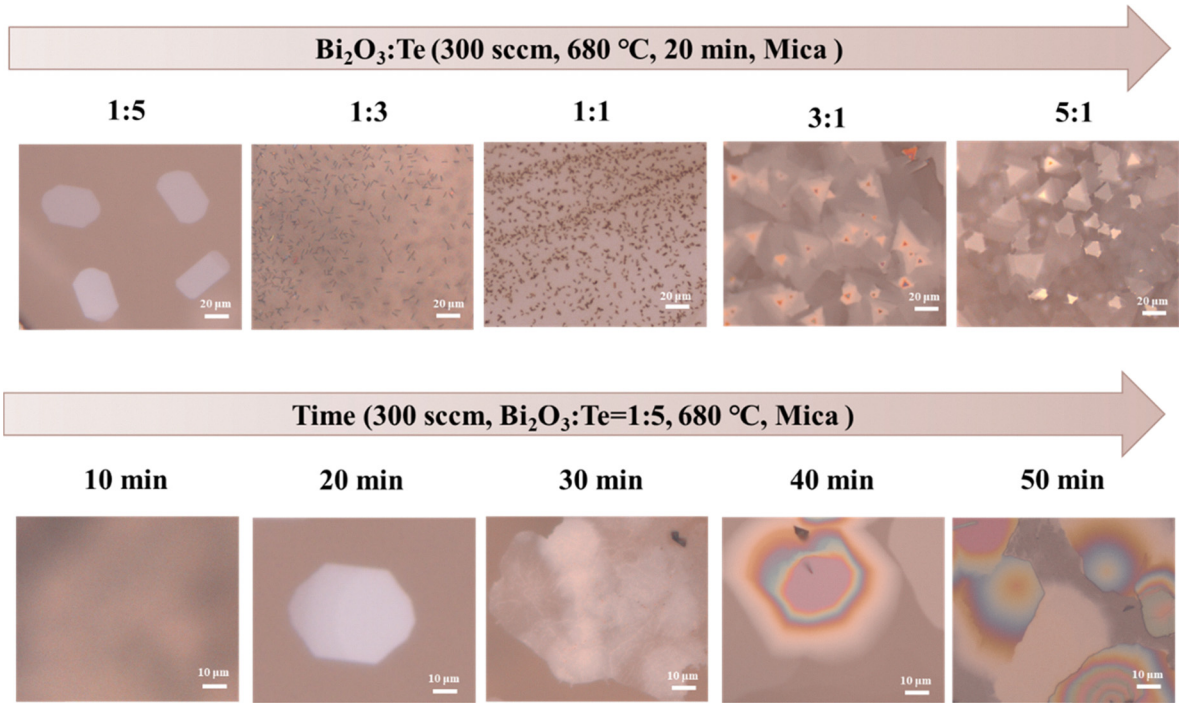

Fig. 2 Bi_2TeO_5 nanosheets grown under different precursor ratios and temperatures.

transferring the tetrahedral nanosheets onto a copper grid resulted in a triangular projection corresponding to the (111) plane. As shown in Fig. S2b, SI, under otherwise identical conditions, increasing the gas flow rate from 100 to 500 sccm yielded Bi_2TeO_5, with the material area increasing with the flow rate. Te nanowires formed at 620 °C, while Bi_2TeO_5 was grown between 650 °C and 750 °C. The thickness of the Bi_2TeO_5 nanosheets grown at 720 °C was higher than that of the Bi_2TeO_5 nanosheets grown at 680 °C. Further temperature increases favored larger nanosheet areas. Finally, substrate choice also influenced the growth. While Bi_2TeO_5 nanosheets formed on both sapphire and mica, those on sapphire were thicker. From the above experimental results, the optimal conditions for obtaining large, uniform Bi_2TeO_5 nanosheets were as follows: growth on mica at 680 °C for 20 minutes under atmospheric pressure with 300 sccm Ar flow and a Bi_2O_3 : Te precursor ratio of 1 : 5.

SHG tests were conducted to determine the non-centrosymmetric and rotationally symmetric structures. Fig. 3a shows the SHG spectrum obtained at room temperature using 800 nm excitation, revealing a distinct 400 nm peak from the sample. For angle-dependent SHG measurements (Fig. 3b), linearly polarized 800 nm light was incident on the sample. The polarization angle (0° defined arbitrarily) was rotated from 0° to 360°, and the SHG intensity at 400 nm was recorded. In order to further explore the response characteristics of Bi_2TeO_5 devices to polarized light, we conducted a detailed polarized light detection study at 365 nm wavelength. Fig. 3b shows the angle-dependent SHG test results. The test results show a two-leaf grass shape, which was consistent with the test results of the bulk Bi_2TeO_5, indicating that the low-dimensional Bi_2TeO_5 nanosheets also have an asymmetric structure and nonlinear optical effects. The results of angle-dependent SHG experiments confirm the existence of spontaneous polarization in Bi_2TeO_5.[30]

Fig. 3c shows the stable maximum photoelectric values extracted at each polarization angle of the incident light, and these values all correspond to the wavelength of 365 nm. The experimental results show that the photocurrent changes periodically with the polarization state. The maximum current I_{max} was 6.04 pA and the minimum current I_{min} was 3.94 pA. Based on these data, the calculated photocurrent anisotropy ratio (the ratio of the maximum photocurrent I_{max} to the minimum photocurrent I_{min}) was only 1.53. When the polarized light angle in the device was from 0° to 90° and from 180° to 270°, the change of the current is relatively gentle. This may mainly be due to the contribution of the shift current, which was caused by the phase difference of the wave function of electrons in the non-centrosymmetric crystal. When the polarized light angle was from 90° to 180° and from 270° to 360°, the current fluctuation was relatively large. This might be due to the contribution of the ballistic current. The asymmetry of the carrier momentum distribution caused by the electron–phonon interaction leads to the generation of current.[31] Meanwhile, the test results show that the angular interval between adjacent maximum and minimum values is not the ideal 45° interval angle, indicating that during the movement of carriers, due to the existence of the depolarization field, the movement trajectory and scattering process are changed.[32]

The *I*–*V* curve under different wavelengths of light is shown in Fig. 3d. The photocurrent generated by the Bi_2TeO_5 device under the irradiation of the 365 nm light source was the strongest, while the photocurrent generated under the

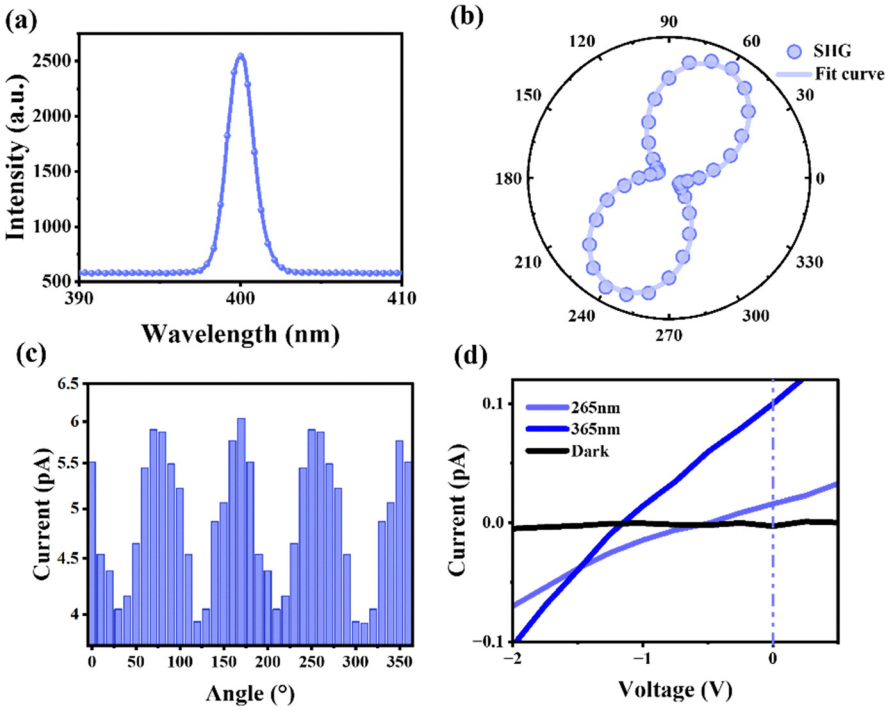

Fig. 3 (a) SHG test of Bi_2TeO_5 nanosheets. (b) Angle-dependent SHG spectra of Bi_2TeO_5 nanosheets. (c) Polar I–θ traces under 365 nm. (d) The I–V characteristic curve of a Bi_2TeO_5 device when exposed to light at different wavelengths.

irradiation of 265 nm was weaker. This test result was also consistent with the test results of UV-visible light absorption and UPS. Under 365 nm illumination, the open circuit voltage (V_{oc}) and short circuit current (I_{sc}) of Bi_2TeO_5 were −1.14 V and 0.1 pA respectively. Under 265 nm illumination, the current increases from −0.06 pA to 0.03 pA in the −2 V to 2 V range, and the V_{oc} and I_{sc} of Bi_2TeO_5 were −0.94 V and 0.01 pA respectively. In the −2 V to 2 V range, the dark current is less than 0.002 pA, which indicates that the current response of 0.01 pA was reliable at 265 nm.

The optical properties of Bi_2TeO_5 nanosheets were thoroughly investigated using ultraviolet photoelectron spectroscopy (UPS) and UV-vis absorption spectroscopy. As depicted in Fig. S3b, SI, the UPS results indicate a cut-off energy (E_{cutoff}) of 15.47 eV and a distance of 0.57 eV between the valence band and the Fermi level (E_F). Using eqn (2)

$$\Phi = h\nu + E_{cutoff} - E_F \quad (2)$$

which involves the Planck constant (h), frequency (ν), and the incident energy ($h\nu$ of about 21.22 eV, as derived from the UPS setup using a helium illuminant), we calculated the work function (Φ) of the Bi_2TeO_5 nanosheets to be 6.32 eV. Fig. S3c, SI displays the UV-vis spectra of the Bi_2TeO_5 nanosheets, with the inset showcasing the Tauc plot. The tangent line of the curve intersects the X-axis at 3.49 eV, revealing a bandgap width of 3.49 eV for the nanosheets. Combining the UPS-derived the valence band maximum (VBM) position (0.57 eV) and the optical band gap (3.49 eV) and assuming the conduction band minimum (CBM) is derived from these values, the band alignment was constructed (Fig. S3d, SI) to obtain the precise locations of VBM, CBM, and the Fermi level. These insights, coupled with the UPS and UV-vis results, allow us to accurately calculate the bandgap of the Bi_2TeO_5 nanosheets. The band structure diagram in Fig. S3d highlights the bandgap characteristics of the Bi_2TeO_5 nanosheets. In comparison with previous experimental results on bulk Bi_2TeO_5, we observe a change in the bandgap width in low-dimensional Bi_2TeO_5, imparting distinct properties to the nanosheets. Notably, the cut-off wavelength of low-dimensional Bi_2TeO_5 materials falls within the ultraviolet range, making them ideal for applications such as photodetectors in the ultraviolet spectrum.

As shown in Fig. 1a, Bi_2TeO_5 was not a traditional layered material. Bi_2TeO_5 was constructed by alternating arrangement of the BiO_5 cage and Te^{4+} atoms in layer A, coupled with Bi^{3+} and O^{2-} atoms in layer B. Bi^{3+} and O^{2-} ions form a wedge-shaped BiO_5 molecular cage in the C-axis direction. The wedge-shaped asymmetric scattering center model suggests that randomly distributed, uniformly oriented wedges in ferroelectrics can generate a net current due to anisotropic carrier scattering and drift. In the absence of applied voltage, the surface of the Bi_2TeO_5 film has a high density of polarized charges, which, if not shielded, will inherently generate an internal electric field (F_p). When the film is in contact with the metal, the polarized charge on the surface of the film will be partially shielded by the free charge in the metal or the semiconductor. In general, the charge on the surface of the film will not be completely shielded because the center of gravity of the polarized charge and the free compensation charge do not coincide, which will generate an electric field inside the entire ferroelectric film, that is, F_{dp}.[33]

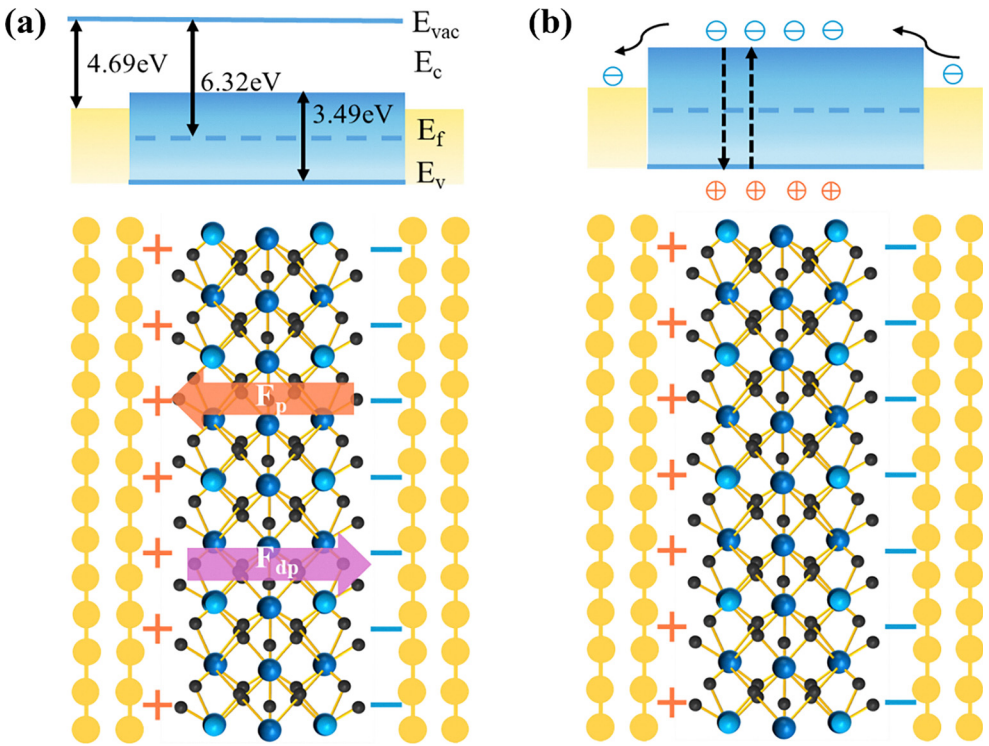

Fig. 4 (a) The polarization charge on the surface of the Bi_2TeO_5 film in the partially shielded state. (b) The internal changes of the Bi_2TeO_5 device after illumination.

As shown in Fig. 4a, when Bi_2TeO_5 was incorporated into a metal/ferroelectric/metal-structured device and interfaced with a TiAu electrode, the polarized charges are partially shielded by free charges and holes residing in the metal, resulting in a F_{dp} within the ferroelectric.[33,34] The F_{dp} produced under 365 nm irradiation was 5.7×10^7 V m^{-1}. The lower the polarized charge shielded, the stronger the depolarization field, and the more efficient the photogenerated carrier separation. The photovoltaic properties of Bi_2TeO_5 were affected by many factors, and there was a certain relationship between these factors. The self-drive of the Bi_2TeO_5 device was the result of the integrated effect of the wedge scattering center structure and the depolarization field. Under illumination, photogenerated carriers are created within the Bi_2TeO_5 lattice. As depicted in Fig. 4b, the asymmetric geometry of the BiO_5 cages makes them act as wedge-shaped scattering centers, inducing directional carrier scattering. This structural asymmetry synergizes with the F_{dp} to cooperatively drive the separation of photogenerated electron–hole pairs. The combined effect significantly enhances photovoltaic current generation. In addition, since the Bi_2TeO_5 nanosheet forms a Schottky barrier with the Ti–Au electrode, the Schottky barrier in the device is calculated using eqn (3).[35]

$$\phi_{Bn0} = \phi_m - \chi \quad (3)$$

where ϕ_m is the work function of the metal and χ is the affinity of the electron; the calculated Schottky barrier ϕ_{Bn0} was 0.06 eV. The Schottky barrier was much lower than the open circuit voltage formed by the 265 nm and 365 nm light sources, which indicates that the influence of the Schottky barrier on the formation of the material open circuit voltage was limited, and the extremely high open-circuit voltage was mainly due to the volumetric photovoltaic effect driven by the depolarization field, rather than the metal/semiconductor interface barrier (only 0.06 eV).

As shown in Fig. S4a and b, SI, Bi_2TeO_5 nanosheets were transferred onto a SiO_2/Si substrate, and Ti–Au electrodes were deposited at both ends of the material to prepare a Bi_2TeO_5 photodetector. According to the AFM data obtained from Fig. S4c, SI, the R_a of the Bi_2TeO_5 material was 1.72 nm; the R_a of the Ti–Au electrode was 2.45 nm; and the R_a of the connection part between the Bi_2TeO_5 material and the Ti–Au electrode was 2.09 nm, which was between the material as a whole and the electrode, indicating that there was good contact between the material and the electrode and the stability was relatively good.

The Bi_2TeO_5 photodetector was also tested under a 265 nm light source to assess its photoelectric performance. Fig. 5a illustrates the I–V characteristic curve of the Bi_2TeO_5 photodetector under varying intensities of 265 nm irradiation. At a bias voltage of 8 V, the dark current stands at a low value of 9.48×10^{-15} A. When the optical power density was 17 μW cm^{-2}, the photocurrent was 4.36×10^{-13} A, an increase of two orders of magnitude. The significant enhancement of photocurrent over dark current across the applied bias range clearly demonstrates the device's photoconductivity effect, where conductivity increases under illumination. The characteristic curve in Fig. S4b, SI illustrates the variation in photocurrent with light power intensity at a bias of 8 V. The photocurrent I_{ph} (eqn (4)) was modeled using a power law equation (eqn (5)).

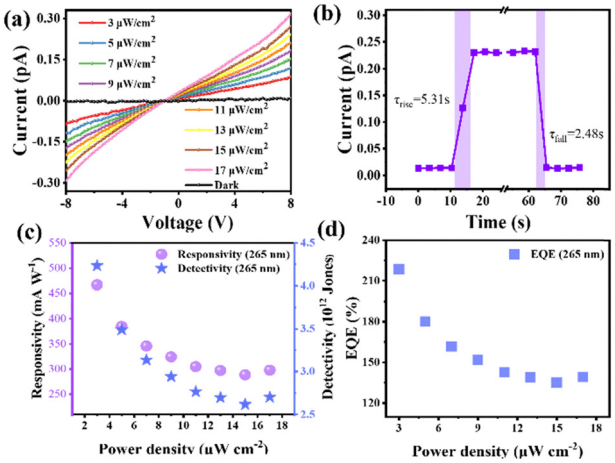

Fig. 5 Photoelectric response under a 265 nm light source. (a) Light response characteristic curves with various light intensities. (b) Response speed. (c) The responsivities and detectivities at different optical powers. (d) The EQE at different optical powers.

$$I_{ph} = I_{light} - I_{dark} \quad (4)$$

$$I_{ph} \propto P^{\theta} \quad (5)$$

where θ represents the fitting index and P denotes the light power intensity. The experimental data yield a fitting index θ of 0.77. The rise time and fall time were 5.31 s and 2.48 s (Fig. 5b). Fig. S4c, SI exhibits the I–t characteristic curve of the Bi_2TeO_5 photodetector when cyclically exposed to 265 nm UV irradiation at 0.01 Hz with a bias voltage of 8 V. Fig. S4d, SI shows the I–t curve under variable power densities, showing good repeatability, stability and periodicity. Responsivity (R) and detectivity (D^*) are crucial metrics for evaluating the photodetector performance. The relevant results calculated are shown in Fig. 5c. As calculated using eqn (6),

$$R = I_{ph}/PA \quad (6)$$

where A is the effective area of the photodetector, the Bi_2TeO_5 photodetector was conducted on a square material area with dimensions of 2.5 μm × 2.5 μm. The R under a power density of 3 μW cm^{-2} was 466.80 mA W^{-1}. As the power density increased, R decreased, likely due to the enhanced scattering and recombination rates of hot carriers within the channel under high-power illumination. The detectivity was calculated using eqn (7).

$$D^* = R\sqrt{\frac{A}{2eI_{dark}}} \quad (7)$$

Here, e is the unit charge and I_{dark} is the current value under dark conditions, which reached 4.23 × 10^{12} Jones under a power density of 3 μW cm^{-2}, indicating the impressive sensitivity of the device. External quantum efficiency (EQE) can measure the ability of the detector to convert incident light into current and is an important parameter to characterize the performance of optoelectronic devices. Using eqn (8), the EQE of the photodetector can be calculated.

$$EQE = Rhc/e\lambda \quad (8)$$

where h is the Planck constant, c is the speed of light, e is the unit charge, and λ is the wavelength of incident light. Through the calculation of this formula, it was ascertained that without the external bias voltage, the EQE under the irradiation of a 365 nm light source was 0.44%, while the EQE under the irradiation of a 265 nm light source with a 0 V bias voltage was 23.1%. When an 8 V bias voltage was increased, the calculated EQE is shown in Fig. 5d. When the light exposure was 3 μW cm^{-2}, the EQE reached 218.44%.

As shown in Fig. S5a, SI, the I–V curve reveals the device's electrical behavior both under dark conditions and under 365 nm illumination. When the bias voltage was set at 8 V, the photocurrent surged to 1.09 × 10^{-12} A, a significant three-order magnitude enhancement over the dark current of 9.48 × 10^{-15} A. When the bias voltage was set at −8 V, the photocurrent was −1.08 × 10^{-12} A, indicating that the Schottky contact has little effect on charge separation in the device. Fig. S5b, SI shows the I–V characteristics of the photodetector under dark conditions and different 365 nm irradiation intensities. As the illumination intensity increased from 0.28 to 12.7 mW cm^{-2}, the current responded accordingly, ranging from 1.40 × 10^{-13} A to 1.09 × 10^{-12} A. Here, the fitting index θ was found to be 0.64 (Fig. S5c, SI). The R under a power density of 0.28 mW cm^{-2} was 76.57 mA W^{-1}, the D was 6.95 × 10^{11} Jones (Fig. S5d, SI), and the EQE was 25.99% (Fig. S5e, SI). The rise and fall times were found to be 2.35 s and 2.26 s respectively (Fig. S5f, SI). The power-dependent I–t curve (Fig. S5g, SI) and the 125-cycle I–t curve (Fig. S5h, SI) show that the device has good repeatability, stability and periodicity. Under identical testing conditions, the photocurrent responses of multiple devices were measured, and an error bar plot was constructed (Fig. S6, SI). This figure clearly demonstrates the consistency in photocurrent response among newly fabricated devices. All measured currents were at the picoampere level, conclusively validating the reliability of the device.

Experimental

Growth and characterization

Using high-temperature tube furnace equipment, we successfully grew Bi_2TeO_5 nanosheets on a substrate. As precursors, bismuth oxide powder (Bi_2O_3, Aladdin, 99.99%) and tellurium (Te, Macklin, 99.99%) were utilized to provide the necessary material source. Te, Bi_2O_3, and the substrate were carefully layered in a clean corundum boat, which was then placed in the high-temperature zone of the tube furnace. To ensure a clean reaction environment, the quartz tube was initially evacuated and then purged with 500 sccm of argon gas. This process was repeated three times to thoroughly clean the reaction zone. Following the cleaning, argon gas was injected into the pipe to maintain the tube under normal pressure. The furnace was then heated to the desired temperature and maintained at this temperature for the corresponding time. After the synthesis, the tube was cooled naturally under a protective argon atmosphere. To characterize the morphology of the Bi_2TeO_5 nanosheets, we

employed an optical microscope (WMX-9688). Additionally, the thickness was analyzed using AFM (Hitachi AFM5500M). The elemental composition and structure were investigated through XPS (ESCALAB 250Xi), XRD (Empyrean S3 X-ray diffractometer), and TEM (Tecnai G2 F20). Lastly, Raman spectroscopy was performed using a confocal micro-Raman system (Renishaw inVia and FST2-Ahdx-DZ) equipped with a monochromator and a 532 nm laser.

Transfer

Bi_2TeO_5 nanosheets were transferred onto a SiO_2/Si substrate, with SiO_2 possessing a thickness of 300 nm. Initially, polymethylmethacrylate (PMMA) was carefully applied to the mica, followed by a baking step at 150 °C for 5 minutes. Subsequently, a polydimethylsiloxane (PDMS) layer was layered over the PMMA, and a further baking procedure was carried out at 50 °C for 5 minutes. Utilizing the hydrophobic separation between PMMA/PDMS and mica, the PMMA/PDMS film was then precisely transferred onto the SiO_2 substrate using a specialized transfer platform. To transfer the Bi_2TeO_5 nanosheets onto a carbon-supported Cu grid, a similar process was followed: PMMA was applied to the mica and baked at 150 °C for 5 minutes. Then, the PMMA and mica were separated *via* hydrophobic techniques. The separated PMMA film, carrying the Bi_2TeO_5 nanosheets, was gently scooped up using a carbon-supported Cu grid. This grid was then dried at 120 °C for 10 minutes to ensure stability. Finally, the Cu grid was soaked in acetone to release and obtain the Bi_2TeO_5 nanosheet samples, ready for subsequent TEM testing.

Device fabrication and measurements

Initially, Bi_2TeO_5 nanosheets were transferred from the mica substrates to the SiO_2/Si substrates. Polymethyl methacrylate (PMMA) was evenly spin coated on the substrate with the sample. Subsequently, the electrode pattern was precisely prepared using the advanced electron beam lithography technology (eBL, eLINE Plus, Raith). As a culminating step, a layered deposition of Ti (10 nm) and Au (30 nm) was carried out on the SiO_2 substrates *via* thermal evaporation, resulting in robust electrical contacts. To evaluate the electrical properties of these devices, a comprehensive assessment was conducted using a probe station (HFS600E-PB4) and a semiconductor device parameter analyzer (Keithley 4200A-SCS, Keithley 4200-PA Remote Preamp Module). All measurements were executed under standard room temperature and atmospheric pressure conditions.

Conclusions

In summary, a high-quality low-dimensional Bi_2TeO_5 material was successfully synthesized *via* the CVD method, achieving a band gap width adjustment from 3.21 eV in the bulk form to 3.49 eV in its low-dimensional state. The Bi_2TeO_5 photodetector had extremely high EQE and detection rate. This study establishes the feasibility of low-dimensional Bi_2TeO_5 materials in the field of photoelectric detection and provides a new and exciting angle for the research of high-performance photodetectors and ultra-low dark current photodetectors, which is expected to open up a new avenue for technological progress.

Author contributions

Yunxiao Min: data curation (equal) and writing the original draft (equal). Jie Liu: data curation (equal) and visualization (equal). Zihan Wang: investigation (equal) and validation (equal). Liang Li: funding acquisition (lead) and writing – review and editing (equal).

Conflicts of interest

There are no conflicts to declare.

Data availability

The data supporting this article have been included as part of the Supplementary Information. See DOI: **https://doi.org/10.1039/d5tc01483b**. The Supplementary Information provides supporting data for the synthesized Bi_2TeO_5 nanosheets and their photodetector application. It includes material characterization (Raman, EDS), growth process details, and optical/electronic property analyses (SHG, UPS, band structure). Furthermore, it presents comprehensive device schematics and performance metrics for the photodetector, such as photoresponse, stability, and efficiency under various light conditions.

Acknowledgements

The National Key R&D Program of China (Grant No. 2023YFE0210800), the Pioneer Hundred Talents Program of the Chinese Academy of Sciences (Grant No. E24BHD17) and the HFIPS Director's Fund (Grant No. YZJJ202404-CX) are acknowledged.

References

1 D. Li, J. K. Qin, B. X. Zhu, L. Q. Yue, S. Qiang, C. Y. Zhu, P. Y. Huang, L. Zhen and C. Y. Xu, *Adv. Funct. Mater.*, 2024, 2417619.
2 D. Akinwande, C. Huyghebaert, C. H. Wang, M. I. Serna, S. Goossens, L. J. Li, H. S. P. Wong and F. H. L. Koppens, *Nature*, 2019, **573**, 507.
3 M. Chhowalla, D. Jena and H. Zhang, *Nat. Rev. Mater.*, 2016, **1**, 16052.
4 S. Ghosh, Y. Zheng, M. Rafiq, H. Ravichandran, Y. Sun, C. Chen, M. Goswami, N. U. Sakib, M. U. K. Sadaf, A. Pannone, S. Ray, J. M. Redwing, Y. Yang, S. Sahay and S. Das, *Nature*, 2025, **642**, 327–335.
5 X. Zhou, X. Z. Hu, J. Yu, S. Y. Liu, Z. W. Shu, Q. Zhang, H. Q. Li, Y. Ma, H. Xu and T. Y. Zhai, *Adv. Funct. Mater.*, 2018, **28**, 1706587.
6 A. K. Geim and I. V. Grigorieva, *Nature*, 2013, **499**, 419.

7 D. Alagarasan, S. Varadharajaperumal, K. Deva Arun Kumar, R. Naik, S. Umrao, M. Shkir, S. AIFaify and R. Ganesan, *Opt. Mater.*, 2021, **121**, 111489.
8 S. Supriya, P. C. Kumar, M. Pradhan and R. Naik, *ACS Appl. Mater. Interfaces*, 2024, **16**, 33806–33818.
9 D. Alagarasan, S. Varadharajaperumal, K. D. A. Kumar, R. Naik, A. Arunkumar, R. Ganesan, G. Hegde, E. El and S. Massoud, *Opt. Mater.*, 2021, **122**, 111706.
10 S. Goossens, G. Navickaite, C. Monasterio, S. Gupta, J. J. Piqueras, R. Pérez, G. Burwell, I. Nikitskiy, T. Lasanta, T. Galán, E. Puma, A. Centeno, A. Pesquera, A. Zurutuza, G. Konstantatos and F. Koppens, *Nat. Photonics*, 2017, **11**, 366.
11 Y. Liang, Y. Chen, Y. Sun, S. Xu, J. Wu, C. Tan, X. Xu, H. Yuan, L. Yang, Y. Chen, P. Gao, J. Guo and H. Peng, *Adv. Mater.*, 2019, 1901964.
12 Q. Fu, C. Zhu, X. Zhao, X. Wang, A. Chaturvedi, C. Zhu, X. Wang, Q. Zeng, J. Zhou, F. Liu, B. K. Tay, H. Zhang, S. J. Pennycook and Z. Liu, *Adv. Mater.*, 2019, **31**, 1804945.
13 P. Luo, F. Zhuge, F. Wang, L. Lian, K. Liu, J. Zhang and T. Zhai, *ACS Nano*, 2019, **13**, 9028.
14 U. Khan, Y. T. Luo, L. Tang, C. J. Teng, J. M. Liu, B. L. Liu, H. M. Cheng, D. W. Shen, Y. L. Chen, X. M. Xie and M. H. Jiang, *Adv. Funct. Mater.*, 2019, **29**, 1807979.
15 G. C. Wang, F. J. Liu, R. C. Chen, M. X. Wang, Y. X. Yin, J. Zhang, Z. Sa, P. S. Li, J. C. Wan, L. Sun, Z. T. Lv, Y. Tan, F. Chen and Z. X. Yang, *Small*, 2023, **20**, 2306363.
16 C. Y. Hong, Y. Tao, A. M. Nie, M. H. Zhang, N. Wang, R. P. Li, J. Q. Huang, Y. Q. Huang, X. M. Ren, Y. C. Cheng and X. L. Liu, *ACS Nano*, 2020, **14**, 16803–16812.
17 I. Földvári, R. S. Klein, G. E. Kugel and Á. Péter, *Radiat. Eff. Defects Solids*, 1999, **151**, 145–149.
18 H. Chen, R. Li, C. Ge, X. Ge and W. Xu, *J. Cryst. Growth*, 2005, **281**, 303–309.
19 C. A. López, E. Bâati, M. T. Fernández-Díaz, F. O. Saouma, J. I. Jang and J. A. Alonso, *J. Solid State Chem.*, 2019, **276**, 122–127.
20 K. M. Ok, N. Bhuvanesh and P. S. Halasyamani, *Inorg. Chem.*, 2001, **8**, 1978.
21 R. Montenegro, Z. Fabris, D. A. Capovilla, I. de Oliveira, J. Frejlich and J. F. Carvalho, *Opt. Mater.*, 2019, **94**, 398.
22 J. F. Carvalho, Z. Fabris, I. de Oliveira and J. Frejlich, *J. Cryst. Growth*, 2014, **401**, 795.
23 I. de Oliveira, D. A. Capovilla, J. F. Carvalho, R. Montenegro, Z. V. Fabris and J. Frejlich, *Appl. Phys. Lett.*, 2015, **107**, 151905.
24 I. de Oliveira, J. F. Carvalho, Z. V. Fabris and J. Frejlich, *J. Appl. Phys.*, 2014, **115**, 163514.
25 B. Chen, X. Wang, J. Li, Q. Xiong and C. Zhang, *J. Mater. Chem. C*, 2018, **6**, 10435.
26 M. Han, C. Wang, K. Niu, Q. Yang, C. Wang, X. Zhang, J. Dai, Y. Wang, X. Ma and J. Wang, *Nat. Commun.*, 2022, **13**, 5903.
27 Y. Li, A. Li, C. Wang, M. Han, J. Zhu, Y. Zhong, P. Zhao, G. Song, S. Wang, Z. Shen, L. Wang, H. Zhang, W. Zhou, L. You, W. Ji, J. Lin and L. Kang, *Adv. Funct. Mater.*, 2024, 2421384.
28 P. C. Kumar, G. K. Pradhan, S. Senapati and R. Naik, *ACS Appl. Electron. Mater.*, 2024, **6**, 3311–3324.
29 S. Li, B. Zhang, X. Tian, Z. Zhao, B. Li, Z. Ali, Z. Meng, W. Zhao, L. Peng and Y. Hou, *Nano Lett.*, 2025, **25**(20), 8390–8398.
30 Y. Li, J. Fu, X. Mao, C. Chen, H. Liu, M. Gong and H. Zeng, *Nat. Commun.*, 2021, **12**, 5896.
31 Z. Dai and A. M. Rappe, *Chem. Phys. Rev.*, 2023, **4**, 011303.
32 X. Chen, K. Xu, X. Zhang, H. Liu and Q. Xiong, *Acta Phys. Sin.*, 2023, **72**, 237201.
33 D. Kim, J. Jo, Y. Kim, Y. Chang, J. Lee, J.-G. Yoon, T. Song and T. Noh, *Phys. Rev. Lett.*, 2005, **95**, 237602.
34 R. Mehta, B. Silverman and J. Jacobs, *J. Appl. Phys.*, 1973, **44**, 3379.
35 J. Meng and Z. Li, *Adv. Mater.*, 2020, **32**, 2000130.

